# Characterization of the microstructure and phase equilibria calculations for the powder metallurgy superalloy IN100

Agnieszka M. Wusatowska-Sarnek[a)]
*Department of Metallurgy and Materials Engineering, Institute of Materials Science, University of Connecticut, Storrs, Connecticut 06269-3136*

Gautam Ghosh and Gregory B. Olson
*Department of Materials Science and Engineering, Northwestern University, Evanston, Illinois 60208-3108*

Martin J. Blackburn and Mark Aindow
*Department of Metallurgy and Materials Engineering, Institute of Materials Science, University of Connecticut, Storrs, Connecticut 06269-3136*

(Received 28 March 2003; accepted 14 August 2003)

The microstructure of the Ni-based superalloy IN100 processed by a powder metallurgy route was evaluated to reveal the structures, volume fractions, distributions, and chemistries of the various phases present. These data were compared with those predicted by computational thermodynamics. It is shown that the microstructural parameters expected on the basis of global equilibrium conditions differ significantly from those measured experimentally. However, modification of these calculations by use of constrained and successive equilibria compensated for kinetic effects and led to accurate (or better) predictions of phase volume fractions and chemistries in this alloy. This demonstrated that such modified phase equilibria calculations could be powerful tools for modeling microstructures, even in complex multicomponent alloys processed under nonequilibrium conditions.

## I. INTRODUCTION

Nickel-based superalloys are widely used in situations requiring superior strength at high temperatures and consequently find extensive application in the hot sections of gas turbine and rocket engines and nuclear reactors. A large number of publications have appeared over the 40-year history of these alloys including a regular series of conference proceedings[1] that cover the structural, processing, and performance characteristics of these materials. The reader is referred to such articles for the general background of the project described here. This current work was performed on one of the oldest superalloys, IN100, developed in the early 1960s, but still used today in the cast or powder metallurgy (P/M) forms. Powder processing results in remarkable chemical and structural homogeneity and excellent strength and toughness properties, but poorer creep and rupture capability restricts application at the highest temperatures. Thus, the P/M form of IN100 is used mainly in jet engines for parts operating in the intermediate temperature regime, especially for components such as disks, spacers, and seals.

The two major phases present in IN100 alloy are the ordered $\gamma'$ ($Ni_3Al$-type) phase together with a disordered solid-solution $\gamma$ matrix; the relative volume fractions are approximately 60:40. Carbides and borides occur as minor phases. The strength of this class of superalloys depends on a number of interrelated microstructural parameters including the volume fraction, particle size, distribution, and chemical characteristics of the $\gamma'$ precipitates coupled with the grain sizes of both the $\gamma'$ and $\gamma$ phases.[2] This paper deals with materials processed to give a high-strength condition, achieved by maintaining the material below the $\gamma'$ solvus of about 1460 K, that is, in the two-phase ($\gamma' + \gamma$) field, for all stages of the fabrication cycle, resulting in a fine-grained structure. The evolution of the structural features during this cycle will be covered in a future paper; here we will concentrate on the fully heat-treated state arrived at after subsolvus solution treatment and two aging steps. In this condition the alloy exhibits three sizes of $\gamma'$ precipitates: primary $\gamma'$, the size and distribution of which is set at the solution treatment temperature; secondary $\gamma'$ formed during cooling from annealing temperature; and tertiary $\gamma'$ formed during aging.

[a)]Address all correspondence to this author.
Present address: Pratt & Whitney, 400 Main Street M/S 114-40, East Hartford, CT 06108.
e-mail: wusatoa@pweh.com

 © 2003 Materials Research Society 

Computational thermodynamic codes have developed rapidly in the last decade and now permit the prediction of phase fractions and compositions under equilibrium conditions. The ThermoCalc[3] software, developed by Royal Institute of Technology (Sweden), is used extensively for such calculations. To date, ThermoCalc computations have been used to determine equilibrium phase diagrams,[4,5] critical liquidus and solidus temperatures,[5] and volume fractions of phases[5] for Ni-based superalloys. However, commercial alloys undergoing multiple heat treatments over relatively short periods of time rarely achieve true equilibrium. As a result, the information obtained from global thermodynamic equilibrium calculations may not be applicable to the specific heat treatment conditions. Therefore, in addition to considering global equilibrium conditions, our goal was to extend calculations to various restricted equilibria situations and to compare the results of these calculations with the experimental data. To increase the accuracy of the analysis, the existing relevant databases (thermodynamic and mobility) were extended to include the element vanadium.

The ability to predict accurately the evolution of phase structure and chemistries during processing will greatly improve accuracy and speed in the early stages of designing new materials. Based on this premise, the objective of this research is to establish a calibrated thermodynamic system by comparing computed results with comprehensive microstructural data (sizes, volume fractions, chemical compositions, and distributions of the phases) obtained from P/M processed IN100. This study is but one element of the comprehensive Accelerated Insertion of Materials (AIM) Defense Advance Research Projects Agency (DARPA, East Hartford, CT) project led by Pratt & Whitney.

## II. EXPERIMENTAL

### A. Material

The P/M IN100 material studied in this investigation was extracted from a fully processed component provided by Pratt & Whitney. The chemical composition of the specific alloy studied is given in Table I. Heat treatment consisted of a subsolvus solution treatment, at 1416 K, followed by a two-step aging sequence wherein the material is held at 1255 K and then 1005 K to develop fully the strengthening phases. It should be noted that features of the secondary and tertiary $\gamma'$ phases depend on the local thermal cycle experienced in the part, and as such, is determined by the component section size: the results cited here are for a relatively thin turbine element.

TABLE I. Chemical composition (in wt.%) of the IN100 alloy evaluated.

| Al | Mo | Ti | V | Cr | Co | Ni | Zr | B | C |
|---|---|---|---|---|---|---|---|---|---|
| 4.91 | 3.18 | 4.32 | 0.75 | 12.40 | 18.38 | 56.06 | 0.07 | 0.02 | 0.07 |

### B. Microstructural characterization methods

Conventional metallographic, x-ray, and analytical electron microscopy procedures were used to elucidate morphological and chemical features of phases. Measurements were made after highlighting the target phase by selective etching: for example, Kalling's reagent was used to reveal $\gamma$ matrix grain boundaries unambiguously, $\gamma'$ particles were clearly defined after etching in glycerygia, and carbides were tinted by electroetching in metholic $HClO_4$. A detailed description of the techniques used for morphological studies is the subject of separate publication.[6] A series of representative secondary electron micrographs (corresponding to an area of approximately 1500 $mm^2$ in each case) were recorded in a field-emission scanning electron microscope (JEOL 6335F, Tokyo, Japan). Areas of phases were measured utilizing the National Institutes of Health, Bethesda, MD Scion Image software and converted to diameters under the assumption that the area of a circumscribed circle accurately approximates the dimensions. The volume fractions of the phases of interest were determined by a standard point count method. Characterization of tertiary $\gamma'$, and to some extent secondary $\gamma'$, was performed by transmission electron microscopy (TEM; Philips EM420, Eindhoven, The Netherlands). Thin foils were prepared in a Tenupol (Struers, Copenhagen, Denmark) twin-jet electropolishing apparatus. A solution of 150-ml perchloric acid and 900 ml ethanol at −10 °C was used at an applied voltage of 19 V.

The chemistry of the $\gamma'$ phase was measured *in situ* from bulk samples using energy dispersive x-ray spectroscopy (EDS) with a KEVEX 5100 (Kevex, San Carlos, CA) EDS unit in Amray 1000A (Amray, Bedford, MA) SEM operating at 20 kV. The quantitative chemical evaluation was performed using a standard prepared by resolutioning at 1480 K (i.e., above the solvus temperature) for 15 min and rapidly quenching in water to minimize formation of the $\gamma'$ phase during cooling. In this procedure some decomposition could not be avoided, but was on a scale that did not compromise the chemical measurements. To provide the most accurate data, the $\gamma'$ phase was extracted and standard chemical analysis performed on the residue. Electroetching in an aqueous solution of 1% citric acid and 1% ammonium sulfate at 1.6 V for 5 h preferentially dissolves the $\gamma$-phase leaving the $\gamma'$ particles in relief and these can be scraped from a surface of a sample.[7,8] The chemistry of the extracted $\gamma'$ was determined by inductively coupled plasma spectrometry (ICP). The chemistry of carbides and borides was determined from particles extracted on carbon replicas using EDS in the TEM.

### C. Phase stability calculations

Computational thermodynamics can be a powerful tool for the prediction and understanding of microstructural evolution (phase fraction and composition of the

phases) during complex isothermal treatments such as those used for the alloy studied here. The expanded availability of the ThermoCalc and DICTRA[9] codes coupled with growing and more complete databases have greatly expanded the fidelity of such calculations. In this study, the database of Saunders[10] for nickel-based alloys was used, modified to include vanadium,[11] and ThermoCalc software was used to predict the multicomponent phase fractions and compositions present in IN100. Computational procedures may be modified to provide the most realistic simulation of the structures produced by standard processing of the alloy, and these constrained equilibrium calculations can capture the influence of kinetic factors of phase formation during the thermal exposure and timeframe of interest. A specific example for superalloys is the formation of topologically close-packed (TCP) phases that can form, but often not in the time/temperature regimes that are encountered during processing and service exposure of these materials. A second modification is the incorporation of sequential equilibria in which the compositions and distribution of phases were considered to be frozen after each element of the process cycle and the next step treated as an independent transformation.

## III. RESULTS

### A. Microstructural parameters

It is difficult to reveal all of the microstructural features in a single picture and thus we will illustrate each structural element separately using the specific preparation procedure that facilitates easy and accurate measurements.

#### 1. Features of the $\gamma$ and $\gamma'$ phases

An example of the general grain structure is shown in Fig. 1(a), in which the lighter areas are the $\gamma$ phase and the darker grains are the primary $\gamma'$ phase. The $\gamma$ matrix grains are equiaxed and rather uniform: the average size is 3.82 $\mu$m. The measured frequency of grain diameters is shown in the histogram in Fig. 1(b), and it can be seen that the distribution is log-normal as represented by the solid curve.

The $\gamma'$ phase is formed at several stages of heat treatment, which is reflected in the three different size distributions that are present, specifically relatively large primary $\gamma'$ particles, intermediate sized cooling (secondary) $\gamma'$ particles, and small aging (tertiary) $\gamma'$ particles. Figure 2 illustrates these three types of $\gamma'$ phase, which appear as the darker structural constituent. Primary $\gamma'$ tends to coarsen during the consolidation and isothermal forging operation with the final size and volume fraction set by the solution treatment practice, which also serves to establish the grain size of the $\gamma$ matrix. On closer examination, however, the microstructure of the primary

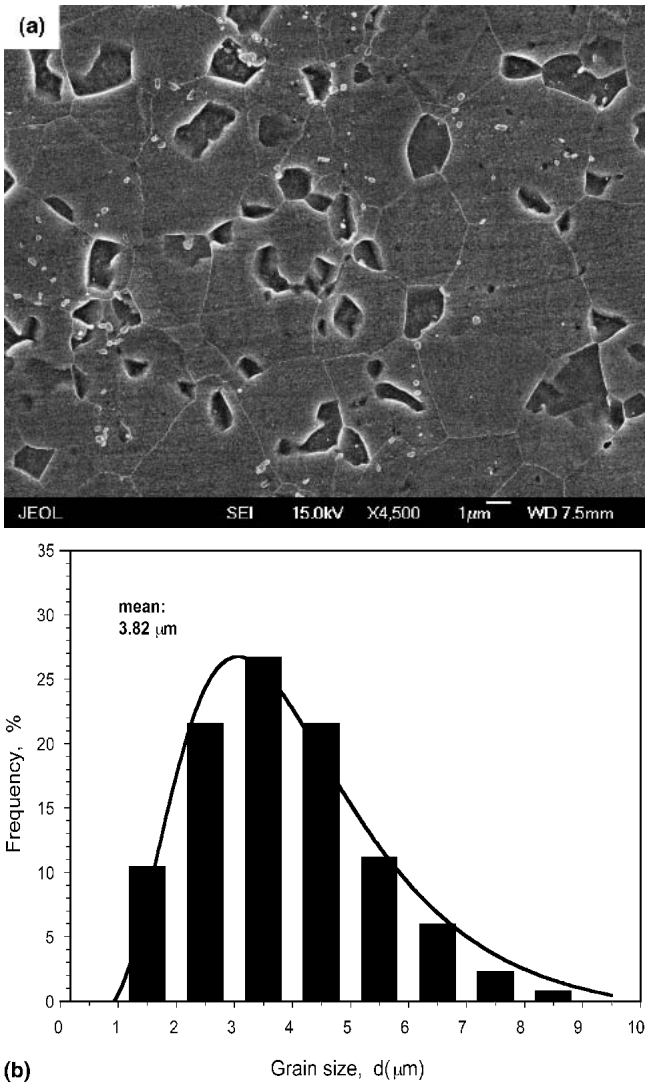


FIG. 1. (a) Secondary electron SEM image of a sample etched using Kalling's reagent showing the main microstructural features: $\gamma$ grain boundaries appear as white lines, darker areas are primary $\gamma'$ phase, and small white particles are carbides. (b) Distribution of $\gamma$ grain size.

$\gamma'$ is more complex; Fig. 3(a) illustrates that the phase typically consists of few impinged $\gamma'$ grains (B) although isolated grains (A) are also observed (confirmed by the phase extraction described below). The number of individual grains that occur in an assemblage rarely exceeds five. Areas of both the individual grains and the agglomerates were measured, and the two distributions are shown in the histograms in Fig. 3(b). It was found that the sizes of the individual particles again follows a log-normal distribution while the spread of the groups of grains is much larger and shows some evidence of subsidiary peaks. The volume fraction of the primary $\gamma'$ was 19.9%.

As mentioned above, the secondary $\gamma'$ particles first form during cooling from the solution temperature, and their morphology and size distributions are strongly cooling-rate-dependent,[4] although the final distributions

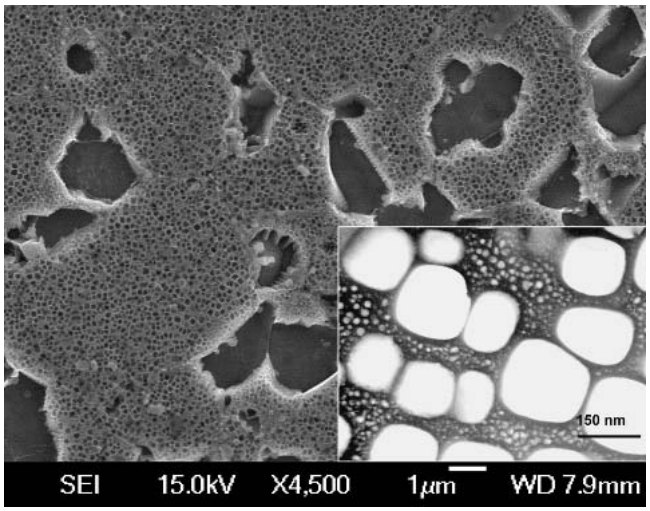


FIG. 2. Secondary electron SEM image of a sample etched using glycerygia, showing two sizes of γ′ phase: large, darker areas are primary γ′ phase and smaller particles are secondary γ′. The inset is a centered dark-field TEM image showing the morphology of secondary and tertiary γ′ particles.

are set by the subsequent aging treatment. Figure 4 shows an example of secondary γ′ morphology; these exhibit a cuboidal shape (average diameter about 120 nm) but with rather rounded corners (radius of curvature approximately 45 nm). The phase is fairly uniformly distributed in the matrix, although we note that there is significant local variation in the width of the γ channel between adjacent secondary γ′ particles. Moreover, in some circumstances there is a denuded zone of up to 180 nm in width at the boundary between the γ grains and the primary γ′ particles (Fig. 6).

The volume fraction of the secondary γ′ particles present in the γ matrix was measured locally within the matrix grain interiors, and then it was recalculated over the total γ′ volume taking into account the primary γ′ volume fraction. This seemingly straightforward procedure proved more challenging than anticipated. The most accurate measure of secondary γ′ particle size was acquired from dark-field TEM micrographs obtained using superlattice 100-type reflections with the γ grain oriented such that the beam direction is approximately parallel to [001]. As with all thin foil measurements, however, projection effects can lead to an overestimate of volume fraction by as much as 15%.[12] The other methods that were used included evaluation of planar surfaces either by direct observation of etched relief or from carbon replicas of such relief. If a standard γ′ etchant such as glycerygia is used, the attack on the particles is quite extensive (Fig. 2) and more than one "layer" of secondary γ′ partcles is sampled. The use of a more dilute etchant reduces the extent of the attack (Fig. 4) and gives a more representative result; however, this tends to lead to an underestimate of the volume fraction due to poorer

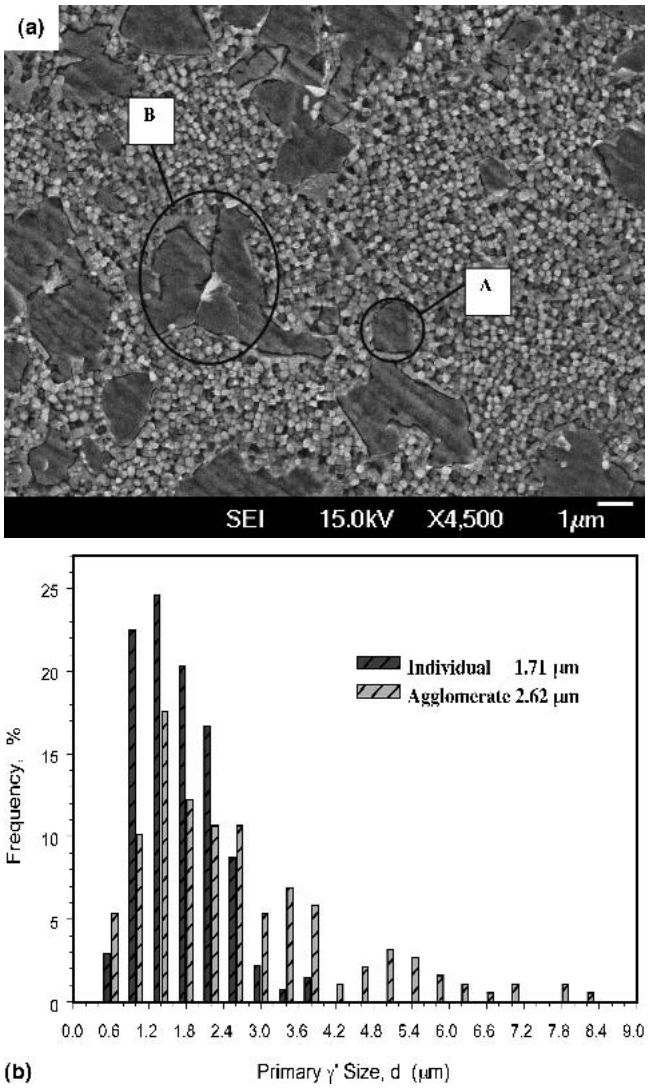


FIG. 3. (a) Secondary electron SEM image of a sample etched using glycerygia followed by anodic dissolution showing isolated grains (A) and multigrain assemblies (B) of primary γ′ particles. (b) Distributions of grain and agglomerate size for primary γ′.

delineation of smaller and/or shallower particles. Taking into account all of these factors, we obtain average values for the volume fraction of secondary γ′ in the range of 26.5% to 33%.

Tertiary γ′ particles achieve their final form during the second aging step and are both small and distributed nonuniformly (Fig. 5). There are narrow denuded zones around the secondary γ′ and the density of the tertiary particles appears to be highest in the wider channels between secondary particles and in the regions adjacent to primary particles (i.e., those regions that are denuded of secondary γ′). The average size of these tertiary particles is 8.5 nm; however, the spread of sizes is large and the maximum size was found to be 17 nm. It was extremely difficult to obtain a reliable or consistent value for the volume fraction of this tertiary γ′ directly; however, this

can be estimated from gravimetric data. In the γ′ extraction experiments, the weight fraction of the separated residue was measured, and this was found to correspond to a volume fraction of 54.5%. Because the total volume fraction of the primary plus secondary γ′ phase was measured to be in the range of 46% to 53%, this would imply that the volume fraction of tertiary γ′ is between 2% and 8%. This is higher than any of the estimates obtained from TEM data. There are many possible reasons for such a discrepancy, including underestimation of the volume fraction from TEM data due to limited resolution in dark-field images or overlap with other γ′ particles[12] and an overestimate of the total volume fraction from gravimetric data due to incomplete dissolution or occlusion of γ phase in the residue. It was not possible to resolve this issue in the current study, but, nevertheless, the gravimetric and metallographic data are in broad agreement.

All the above information is summarized in Table II.

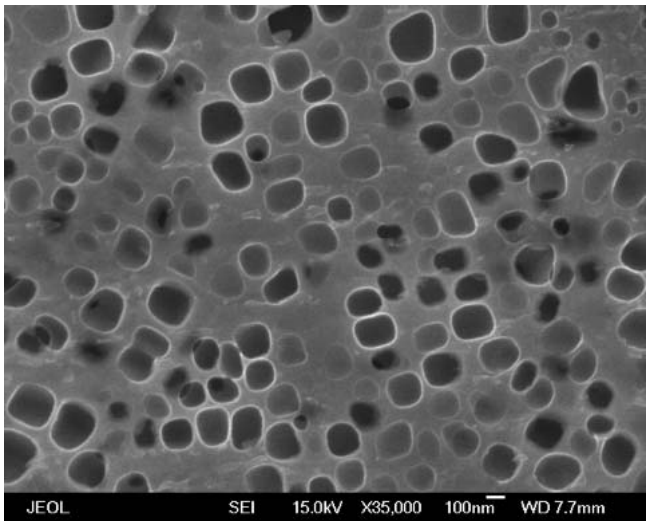


FIG. 4. Secondary electron SEM image of a sample etched using dilute glycerygia showing the morphology of secondary γ′ precipitates.

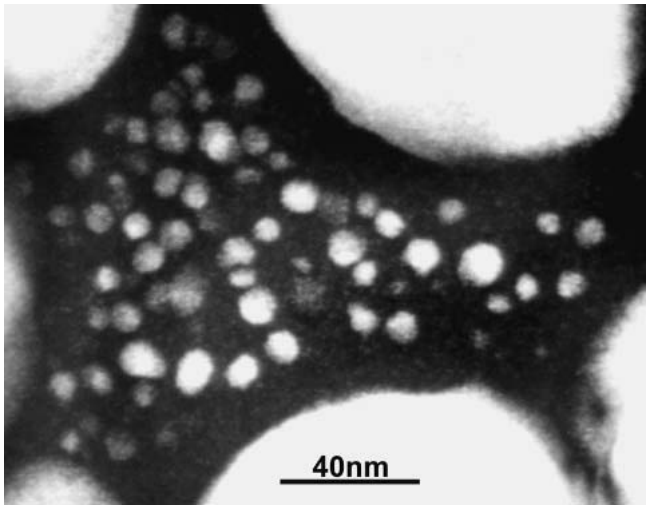


FIG. 5. Centered dark-field TEM image showing the morphology of tertiary γ′ precipitates.

## 2. Phase chemistries of γ and γ′

The composition of γ′ phase was determined from the extracted residue by ICP, and measurements were supplemented by *in situ* EDS of solid samples. It is recognized that the *in situ* quantitative analysis of small particles can be subject to inaccuracies, as the sample volume excited by the electron beam may be comparable with that of the measured phase. For example, at an operating voltage of 20 kV with a sample density of ~8 g/cm$^3$, this volume is about 1 μm$^3$ (Ref. 13). In the investigation, 25 primary γ′ areas with diameters exceeding 2 μm were analyzed.

As the process heat treatment times were relatively short, specimens were exposed for longer times at 1430 K for up to 8 weeks to achieve a state closer to equilibrium. No systematic variation of composition was found, and, furthermore, it was not possible to distinguish between the primary and secondary γ′ chemistries.

Average compositional results from both methods are shown in Table III from which it may be seen that compositions determined by EDS are in good agreement with the results obtained by the ICP method. Based on these values, the chemical formula for γ′ may be written as:

$$(Ni_{0.84}Co_{0.13}Cr_{0.03})_3(Al_{0.55}Ti_{0.31}Cr_{0.07}Mo_{0.04}V_{0.03}) \quad ,$$

with a computed density of 7.72 g/cm$^3$.

TABLE II. Comparison of the measured and predicted volume fractions of γ′ and carbide phases, together with average measured sizes of these phases.[a]

| γ matrix grain size (μm) | γ′ volume fraction (%) | | | | | | Average diameter of γ′ phases | | | Carbide particle size (nm) | Carbides volume fraction (%) | |
|---|---|---|---|---|---|---|---|---|---|---|---|---|
| | Primary | | Secondary | | Tertiary | | Primary (μm) | Secondary (nm) | Tertiary (nm) | | | |
| | Measured | Predicted | Measured | Predicted | Measured | Predicted | | | | | Measured | Predicted |
| 3.82 ± 0.26 | 19.9 ± 2.2 | 20.7 | 30.5 | 27.7 | | 12.4 | 1.71 ± 0.15 | 120.2 ± 7.3 | 8.5 ± 1.2 | 240 | 1.6 | 0.83 |

[a]The predicted volume fractions of γ′ and carbides phases are taken for the *successive equilibria* (case IV) calculation.

TABLE III. Chemical composition (in wt.%) of primary γ′ phase measured by EDS and total γ′ measured by ICP, together with predicted values for case IV.[a]

| | Al | Mo | Ti | V | Cr | Co | Ni |
|---|---|---|---|---|---|---|---|
| Measured | | | | | | | |
| Primary γ′ (EDS) | 6.2 | 1.5 | 7.1 | 0.7 | 3.6 | 12.1 | Balance |
| γ′ phase (ICP) | 6.8 | 1.6 | 7.6 | 0.8 | 4.1 | 11.8 | Balance |
| Predicted | | | | | | | |
| Primary γ′ phase | 7.04 | 0.54 | 8.24 | 0.36 | 3.01 | 13.90 | Balance |

[a]The thermodynamic predictions are the weighted average of the three types of γ′ phase.

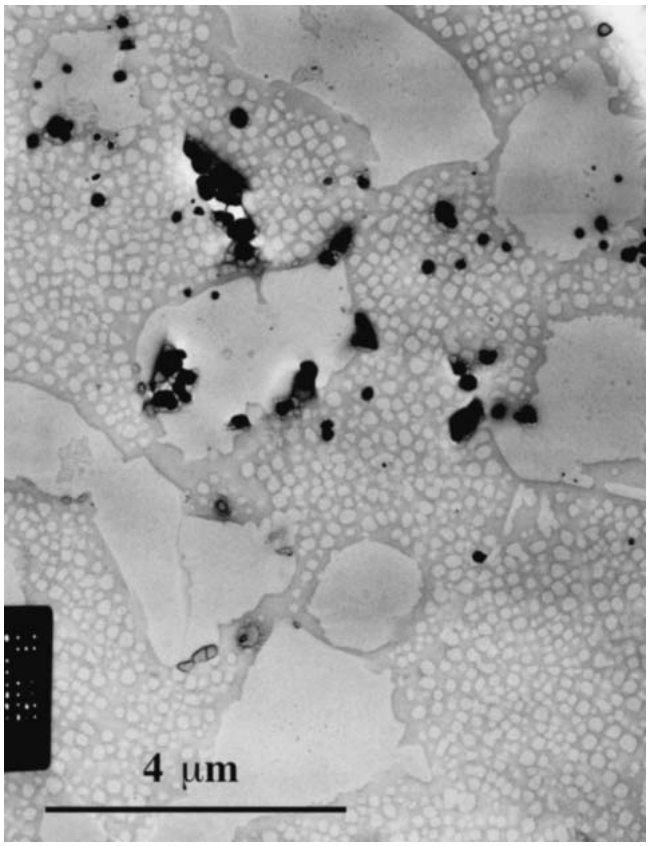


FIG. 6. Bright-field TEM image from a carbon extraction replica showing the distribution of carbides. The spherical particles are MC-type whereas the blocky and elongated ones are $M_{23}C_6$-type.

### 3. Minor phases

The minor phases present in the alloy are mainly carbides with smaller quantities of borides. Figure 6 illustrates the size and distribution of these constituents in an extraction replica; the total volume fraction was measured at approximately 1.6%. Chemical analyses performed by EDS showed that the elongated carbides located at grain boundaries are $M_{23}C_6$-type while the larger, more randomly distributed spherical particles were MC-type. There is some evidence that the MC-type carbides tend to cluster in bands that are associated with prior particle boundaries.[14] Table IV shows the volume fractions and chemistries of both types of carbides together with similar information on the borides.

## B. Phase transformation and chemistry analytical results

### 1. Refinement of the thermodynamic database for vanadium

The current (Saunders) Ni-database[10] does not contain the element vanadium. It was beyond the scope of this program to evaluate all pertinent V-containing binary systems to yield a complete solution, but to provide some partitioning information for V between the γ and γ′ phases the Ni–V and Ni–Al–V (partial) phase diagrams were modeled. Details will be published elsewhere.[11] Figure 7 shows the calculated Ni–V phase diagram, and because the Saunders Ni-database utilizes a two-sublattice model for the σ phase, we have also used the same model. This differs from the three-sublattice model for σ phase proposed by the CALPHAD community.[15] It can be seen that the solubility of V in Ni is fairly substantial at temperatures relevant to the heat treatment of IN100; but it is important to note that the $Ni_3V$ phase is not an equivalent $L1_2$ phase. Rather, it exhibits a tetragonal $DO_{22}$ ($Al_3Ti$-type) structure, based on a related faulted fcc lattice.

Modeling of the Ni-corner of the Al–Ni–V system was performed to define the partitioning of V in γ and γ′. Figures 8(a) and 8(b) show the calculated isothermal

TABLE IV. Chemical compositions, lattice parameters, and measured and predicted volume fractions of minor constituents present in the IN100.[a]

| | Lattice parameter (nm) | Volume fraction (%) | Metal site fraction (at. wt.) | | | | | | | |
|---|---|---|---|---|---|---|---|---|---|---|
| | | | Cr | Mo | Ni | Co | Zr | V | Ti | Al |
| $M_{23}C_6$ | 1.0665 | Measured 1.13 | 0.728 | 0.071 | 0.065 | 0.041 | 0.024 | 0.028 | 0.016 | 0.027 |
| | | Predicted 0.026 | 0.794 | 0.126 | 0.039 | 0.041 | … | … | … | … |
| MC | 0.4311 | Measured 0.50 | 0.024 | 0.089 | 0.033 | 0.010 | 0.029 | 0.027 | 0.753 | 0.035 |
| | | Predicted 0.65 | 0.011 | 0.007 | … | … | 0.202 | … | 0.961 | … |
| $M_3B_2$ | $a_0$ = 0.5784 | Measured Traces | 0.416 | 0.273 | 0.059 | 0.019 | 0.057 | 0.063 | 0.034 | 0.079 |
| | $c_0$ = 0.3125 | Predicted 0.007 | 0.0339 | 0.659 | … | 0.002 | … | … | … | … |
| | c/a = 0.54 | | | | | | | | | |

[a]The predicted volume fractions of minor constituents are taken for the successive equilibria (case IV) calculation.

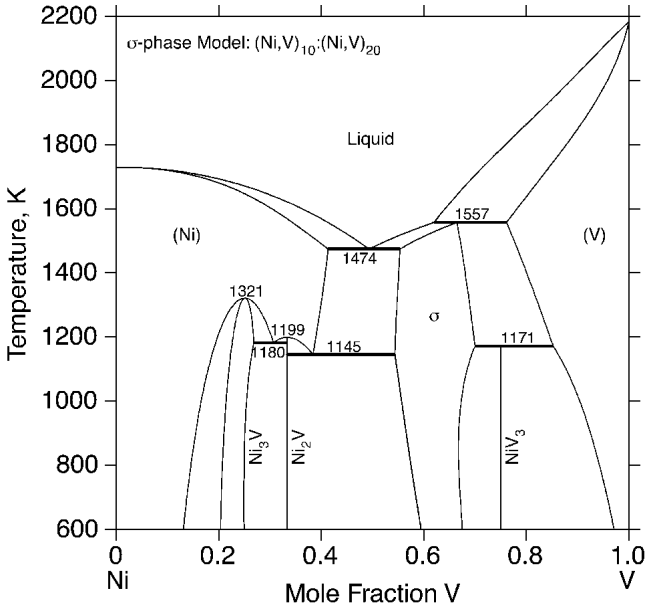


FIG. 7. The calculated Ni–V phase diagram.

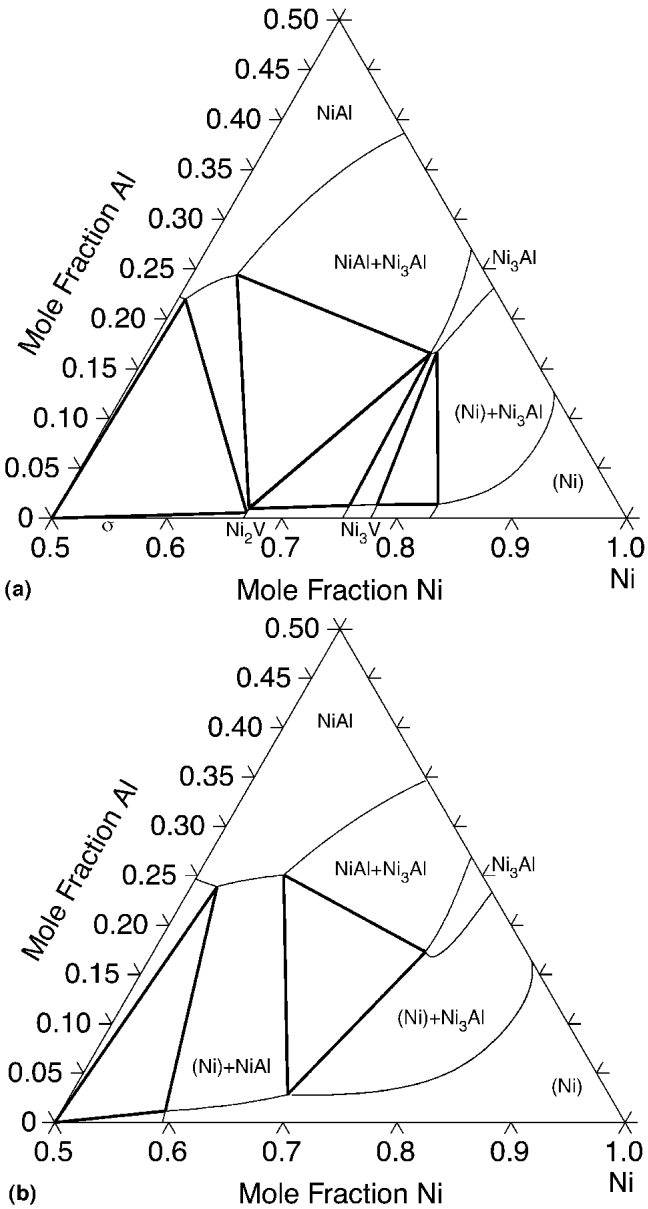


FIG. 8. Calculated isothermal section (partial) of Al–Ni–V at (a) 1073 K and (b) 1373 K.

sections (partial) of this system at 1073 K and 1373 K. It is seen that $\gamma'$ dissolves about 10 at.% V. These calculated Al–Ni–V phase diagrams are consistent with the experimental results of Zapolsky *et al.*[16]

## 2. Calculated unconstrained equilibria in IN100

Figure 9 shows the temperature dependence of $\gamma$ and $\gamma'$ phase fractions. As the temperature increases, the fraction of $\gamma'$ decreases while that of $\gamma$ increases and at 1460K, often called the $\gamma'$-solvus temperature, the alloy becomes essentially single phase. The formation of a number of carbides, borides, and intermetallic phases are predicted for the alloy, and the volume fractions of each of these are shown in Fig. 10 as a function of temperature. The fractions of the two intermetallics, $\sigma$ and $\mu$, decrease rapidly with temperature with the $\sigma$–phase stable to approximately 1140 K while the $\mu$ phase is stable to about 1075 K. In contrast, the fraction of $M_{23}C_6$ phase is rather insensitive to temperature, and this carbide is stable to 1295 K; above this temperature, MC is the stable carbide phase. The boride phase $M_3B_2$ is predicted to be present to approximately 1390 K, and above this temperature $MB_2$ phase is stable.

## 3. Calculated constrained equilibria of IN100

The precipitation kinetics of $\sigma$ and $\mu$ phases exhibit classical C-curve kinetics with the most rapid transformation occurring between 1123 and 1173 K. In as-cast alloys, the incubation period for the $\sigma$ phase in this range is around 4 h while in wrought alloys it is up to 150 h.[17] So for the specific isothermal aging schedules utilized for IN100 studied here, the precipitation kinetics of $\sigma$ and $\mu$ phases are sufficiently slow that the phases do not form. An advantage of the ThermoCalc software is that it can readily handle such situations by calculating the metastable equilibrium that will prevail in the absence of selected phase(s).

A series of such constrained equilibria calculations were performed to simulate the effect on structural stability of eliminating the $\sigma$ and $\mu$ phases. In the first step when only these phases were suspended, it was found that the P phase becomes stable. After subsequently suspending the P phase, it was found that the R phase becomes stable, then HCP phases, and then $\alpha$–Cr phase. Like $\sigma$ and $\mu$, P and R phases are also members of the

group of phases known as topologically close-packed (TCP) phases.[18] While the presence of α–Cr has been observed in several Ni-based superalloys, the phase is not found in the version of IN100 in this study. Figure 11 shows the fractions of γ and γ′ phases that are calculated after these modifications. Comparing Figs. 9 and 11, it is seen that the fraction of γ′ phase does not change while that of γ increases appreciably at lower temperatures. This is due to the fact the primary elemental components of σ and μ phases partition preferentially to the γ phase. Since the fractions of $M_{23}C_6$, $M_3B_2$, $MB_2$, and MC are governed by the B and C concentrations, values do not change appreciably in the absence of TCP phase(s). Predicted volume fractions of γ′ phase are also given in

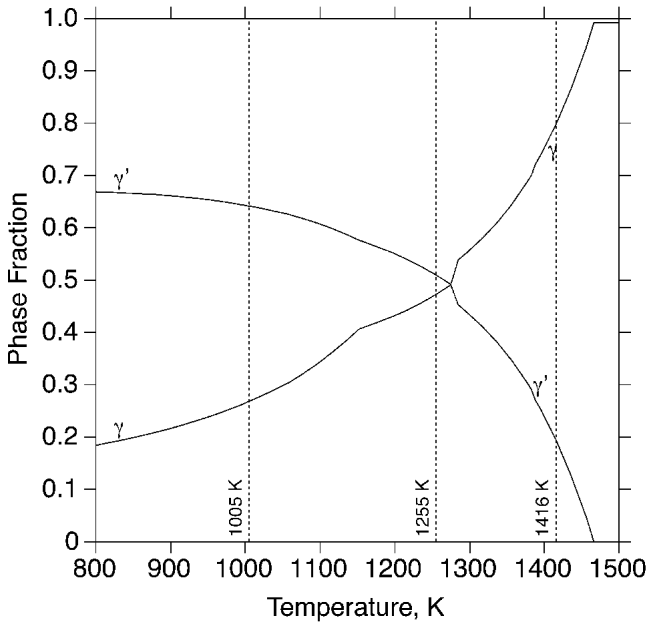


FIG. 9. The calculated volume fractions of γ and γ′ phases as a function of temperature in IN100 under unconstrained conditions (case I).

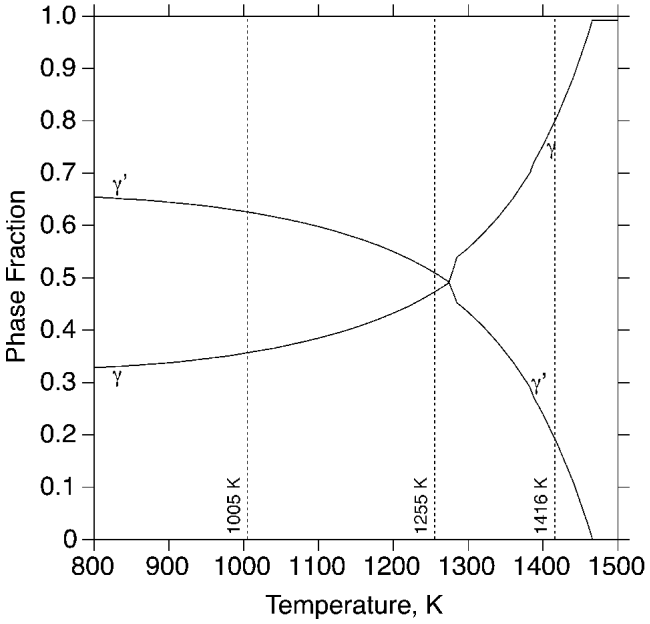


FIG. 11. The calculated volume fractions of γ and γ′ phases as a function of temperature in IN100 under constrained equilibrium conditions (case II).

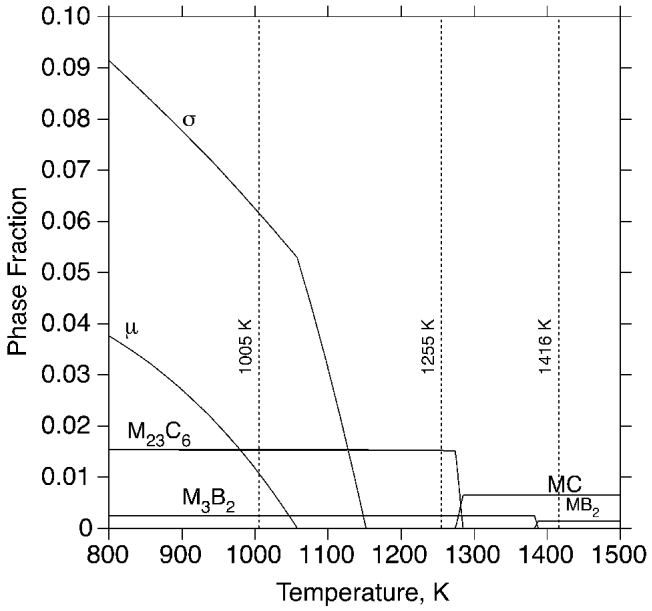


FIG. 10. The calculated volume fractions of borides, carbides, and TCP (σ and μ) phases as a function of temperature in IN100 under unconstrained conditions (case I).

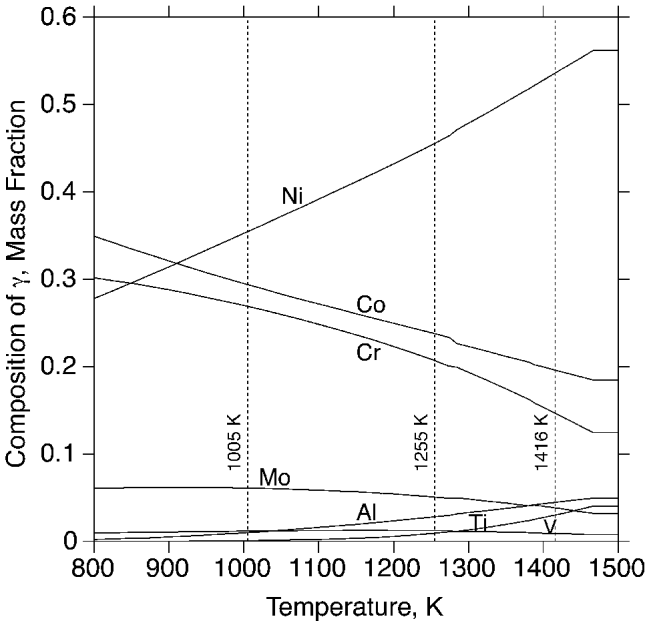


FIG. 12. The calculated composition of γ phase as a function of temperature in IN100 under constrained equilibrium conditions (case II).

Table II and are in good agreement with the experimental values. Figures 12 and 13 show the compositions of the $\gamma$ and $\gamma'$ phases, respectively, under constrained conditions, as a function of temperature. It is seen that the composition of $\gamma'$ is weakly temperature-dependent while Co, Cr, and Ni in $\gamma$ exhibit a strong temperature dependency. Furthermore, compared to the unrestricted equilibrium, there are substantial increases in the Co, Cr, Mo, and Ni contents of the $\gamma$ phase. This again is due to the fact that the formation of TCP phases (rich in Co, Cr, and Mo) has been suppressed.

Comparison of the measured chemistry of the $\gamma'$ and the calculated value is shown in Table III. The general features are clearly captured by the predictions, but deviations in some elements, especially molybdenum, are evident. One possible explanation for the discrepancies is that the measured values are for a nonequilibrated $\gamma'$ phase. To check this possibility, samples were held at 1430 K for up to 8 weeks and the phase compositions monitored as a function of time. Although there were small changes in composition, these seemed to reflect measurement variations rather than any systematic trend to the predicted composition.

The specific features of the final microstructure reflect the several stages of heat treatment. To simulate the phase fractions and compositions formed at various steps of the cycle, we must consider a further type of restricted equilibria that incorporates the concept of successive equilibria. As noted in Sec. II. A, there are three steps in the heat treatment. During the solution treatment step at 1416 K ($T_1$), the alloy undergoes phase redistribution that establishes the primary $\gamma'$ size and fraction ($\gamma'_P$) and sets an initial carbide and boride configuration. During the first aging step at 1255 K ($T_2$), it is considered that all of the precipitates formed at $T_1$ are compositionally frozen (due to insufficient time at $T_2$), and only the matrix at $T_1$ (matrix 1) can undergo further precipitation giving rise to secondary $\gamma'$ ($\gamma'_S$) and potentially other phases. Similarly, at the second aging temperature 1005 K ($T_3$), the precipitates formed at $T_1$ and $T_2$ are assumed to be compositionally frozen, and the matrix established at $T_2$ (matrix 2) undergoes further precipitation giving rise to tertiary $\gamma'$ ($\gamma'_T$) and other phases, if any. Here again the successive equilibria calculations can be performed with or without suspending one or more phases. In other words, it permits the exploration of several possibilities and the results can be calibrated against the experimental data.

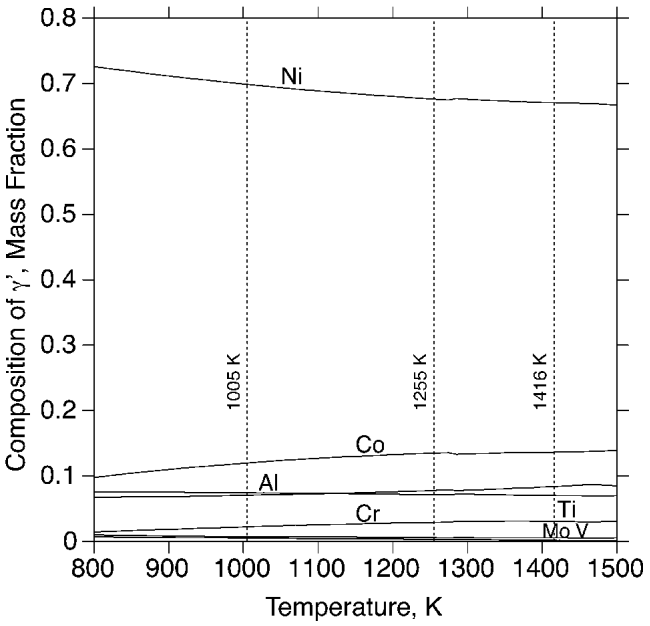


FIG. 13. The calculated composition of $\gamma'$ phase as a function of temperature in IN100 under constrained equilibrium conditions (case II).

Table V summarizes four equilibrium calculations performed for IN100 incorporating the conditions cited above. Both case I and case II represent global equilibria based on bulk-alloy composition, with the TCP phases suspended in case II. Case III and case IV represent successive equilibria considering the matrix composition only, and again, in case IV the TCP phases were not considered.

The phase fractions calculated for these four cases are summarized in Table VI as a function of isothermal heat-treatment temperatures. It is seen that after final heat treatment at 1005 K, the fraction of $\gamma'$ continuously decreases from case I to case IV while that of $\gamma$ increases. The predicted fractions of the primary and secondary $\gamma'$ phases for case IV are in reasonable agreement with the measured values, as shown in Table II. The total $\gamma'$ content, measured by the phase extraction method, appears to correlate well, and the slight difference could be caused by the loss of some of the finest tertiary $\gamma'$ during sample preparation. The carbide phase formed at the solution temperature is correctly predicted to be MC-type, and ancillary experiments have confirmed this is the only carbide present, confirming earlier results on cast alloys.[19] At lower temperatures the $M_{23}C_6$ carbide is found to be the stable form, and this is the dominant phase in the fully heat-treated alloy. For case II, the total fraction of both carbides is in excellent agreement with the calculation, but the experimental results indicate that the transformation of MC to $M_{23}C_6$ is incomplete. Moreover, the existence of the boride phase is predicted correctly.

## IV. COMPARISONS AND DISCUSSION

This paper serves to demonstrate the advances that have taken place in the accuracy of thermodynamic predictions of phase constitution and chemistry in complex alloys. By taking into account the specific aspects of the process cycle experienced by a material, it is

TABLE V. A summary of unrestricted and restricted equilibria calculations performed for IN100.

| | Type of equilibrium | Comments | Restriction |
|---|---|---|---|
| Case I | Global equilibrium | Alloy composition; all phases are considered | None |
| Case II | Global equilibrium | Alloy composition; TCP phases are suspended | Yes |
| Case III | Successive equilibrium | Only matrix composition; all phases are considered | Yes |
| Case IV | Successive equilibrium | Only matrix composition; TCP phases are suspended | Yes |

TABLE VI. Calculated phase fractions ($f_i$) in IN100 corresponding to the unrestricted and restricted equilibria listed in Table 5.

| | | Phase fractions | | | | | | | | |
|---|---|---|---|---|---|---|---|---|---|---|
| Case | Temperature (K) | $f_\gamma$ | $f_{\gamma'}$ | $f_\sigma$ | $f_\mu$ | $f_{MC}$ | $f_{MB2}$ | $f_{M3B2}$ | $f_{M23C6}$ | $\Sigma f_i$ |
| Case I | 1416 | 0.78481 | 0.20720 | ⋯ | ⋯ | 0.00652 | 0.00147 | ⋯ | ⋯ | 1 |
| | 1255 | 0.45581 | 0.52648 | ⋯ | ⋯ | ⋯ | ⋯ | 0.00251 | 0.01520 | 1 |
| | 1005 | 0.24410 | 0.65765 | 0.07149 | 0.00886 | ⋯ | ⋯ | 0.00252 | 0.01540 | 1 |
| Case II | 1416 | 0.78481 | 0.20720 | ⋯ | ⋯ | 0.00652 | 0.00147 | ⋯ | ⋯ | 1 |
| | 1255 | 0.45581 | 0.52648 | ⋯ | ⋯ | ⋯ | ⋯ | 0.00251 | 0.01520 | 1 |
| | 1005 | 0.34151 | 0.64060 | ⋯ | ⋯ | ⋯ | ⋯ | 0.00252 | 0.01540 | 1 |
| Case III | 1416 | 0.78481 | 0.20720 | ⋯ | ⋯ | 0.00652 | 0.00147 | ⋯ | ⋯ | 1 |
| | 1255 | 0.50783 | 0.48405 | ⋯ | ⋯ | 0.00652 | 0.00147 | 0.00006 | 0.00008 | 1 |
| | 1005 | 0.31166 | 0.61702 | 0.04874 | 0.01426 | 0.00652 | 0.00147 | 0.00007 | 0.00027 | 1 |
| Case IV | 1416 | 0.78481 | 0.20720 | ⋯ | ⋯ | 0.00652 | 0.00147 | ⋯ | ⋯ | 1 |
| | 1255 | 0.50783 | 0.48405 | ⋯ | ⋯ | 0.00652 | 0.00147 | 0.00006 | 0.00008 | 1 |
| | 1005 | 0.38365 | 0.60804 | ⋯ | ⋯ | 0.00652 | 0.00147 | 0.00007 | 0.00026 | 1 |

possible to adapt the thermodynamic system to predict the phase structure with remarkable fidelity. The fact that microstructural information is still needed to confirm and calibrate the code results indicates that confidence is building slowly. However, as this type of integrated system expands, introduction of each predictive step into new systems will be accomplished more readily.

Many of the features of the IN100 alloy are captured accurately by the calculations. The strong dependence of the primary $\gamma'$ volume fraction on solution temperature predicted by thermodynamic computations has been verified experimentally, and results are shown for a wider range of temperatures in Fig. 14. It may be noted that, as predicted, the primary $\gamma'$ volume fraction increases rapidly as temperature is reduced from the $\gamma'$ solvus. The total volume fraction of $\gamma'$ is also predicted reasonably precisely, the measured and calculated values differing by less than 3.4% for the case IV prediction. As the agreement between the calculated and measured secondary $\gamma'$ is quite good, the differences appear to be in the tertiary phase content, which, as noted above, is the most imprecise measurement.

The discrepancies between the measured and predicted chemical compositions are perhaps more significant, particularly for certain alloying elements in the $\gamma'$ phase. The predictions underestimate Mo and V contents by over 50% while smaller deviations of about 15% are noted for Cr and Co. Based on the thermal exposure experiments, this cannot be traced to a nonequilibrium condition. One further possibility is that these discrepancies arise due to errors in

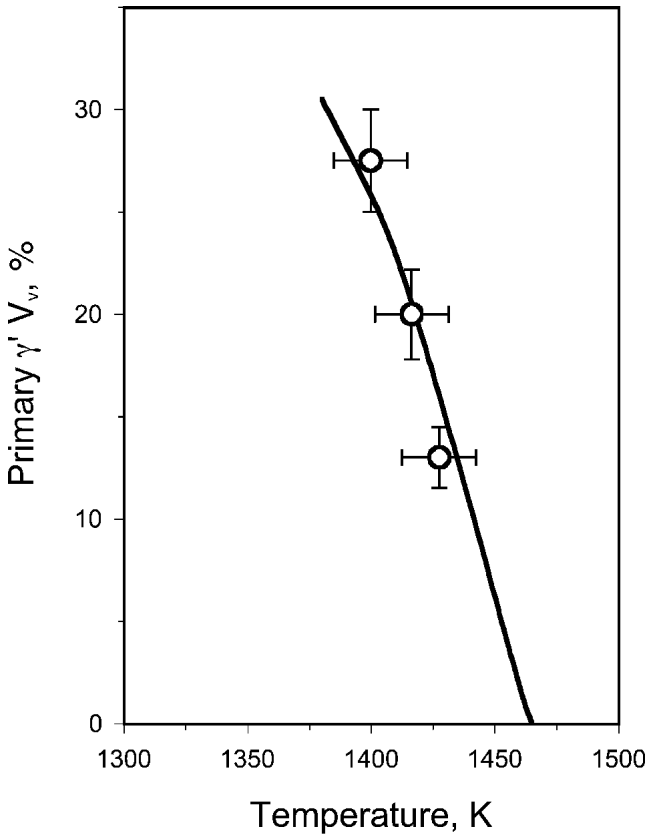


FIG. 14. Variation in the volume fraction of primary $\gamma'$ in IN100 with subsolvus heat-treatment temperature. The points represent experimental data and the solid line is that obtained from the calculations (case II).

the predicted transition metal content in the minor phases. As discussed in Sec. III. B. 2, for case II the predicted volume fraction of the carbide phases is in excellent agreement with that measured experimentally. These volume fractions are, however, determined mainly by the carbon and boron content of the alloy and not by the specific transition metals that the compounds contain. As shown in Table IV, there are differences between the measured and predicted transition metal contents and these could, in turn, influence the predicted $\gamma'$ composition. For example, the calculations predict a much higher Mo content in the $M_{23}C_6$ than that measured experimentally, and this could offset the underestimate in the Mo content of the $\gamma'$ phase.

The present investigation has been extended into the study of the development of microstructure during each step of processing over the range of process parameters encountered in components. The advent of the powerful new PrecipiCalc code[20] can be used to simulate such microstructural evolution, and the comparison of the calculated and measured microstructures will be described in a future paper. A precise prediction of microstructural features and the variation with component configuration and process limits is key input for the modeling of mechanical properties.

## V. SUMMARY

This combined experimental and thermodynamic modeling study was performed on the powder metallurgical Ni-based superalloy IN100 to determine the extent to which the microstructure and phase chemistry of such multicomponent alloys can be predicted. The alloy was subjected to a multistage heat treatment similar to that used for rotors in gas-turbine engines and consists of a majority $\gamma'$ phase, a $\gamma$ solid-solution matrix phase, and several minority carbide and boride phases. The three-step heat treatment results in three distinct length scales of $\gamma'$ phase particles distributed both between and within grains of the $\gamma$ matrix phase. The volume fractions and chemical compositions of the phases were assessed using a variety of metallographic and spectrometric techniques.

In parallel, ThermoCalc routines together with a commercially available thermodynamic database were used to compute the phase volume fractions and compositions. The database was extended to include vanadium. When global equilibrium is assumed, the simulations predict the presence of TCP phases that are not observed experimentally. Such phases in turn influence the volume fractions and compositions of the other phases. The use of constrained equilibria to eliminate such phases with sluggish formation kinetics from the calculation gives a much better match to the data. Moreover, if one uses conditions of successive equilibria to represent limited chemical redistribution during the sequential heat treatments, the calculated parameters correspond very closely to those obtained experimentally. These calculations reflect faithfully the total volume fractions of the $\gamma'$, $\gamma$, carbide, and boride phases, and the main features of the trimodal population of $\gamma'$ are captured. Computed and measured phase chemistries show reasonable agreement although there are some deviations that cannot be explained at this time.

## ACKNOWLEDGMENTS

This work was supported by DARPA/USAF under Contract No. F33615-00-2-5216 with Dr. R. Dutton as technical monitor. The authors acknowledge Pratt & Whitney for providing the materials used in this investigation, for performing the ICP chemistry analysis, and for permission to publish this paper. The authors would also like to thank Larry McCurdy and Dave Horspool for technical support with TEM.

## REFERENCES

1. *Proceedings of the International Symposium on Superalloys I*, TMS, Warrendale, PA, 1968; *ibid* II, 1972; *ibid* III, 1976; *ibid* IV, 1980; *ibid* V, 1984; *ibid* VI, 1988; *ibid* VII, 1992; *ibid* VIII, 1996; *ibid* IX, 2000.
2. C.T. Sims, N.S. Stoloff, and W.C. Hagel, *Superalloys II* (John Wiley & Sons, New York, 1987), pp. 97–133.
3. ThermoCalc, version N (Royal Institute of Technology, Stockholm, 2001).
4. J. Mao, K-M. Chang, W. Yang, K. Ray, S.P. Vaze, and D.U. Furrer, Metall. Trans. A **32A,** 2441 (2001).
5. N. Saunders, *Superalloys VIII – 1996*, edited by R.D. Kissinger, D.J. Deye, D.L. Anton, A.D. Cetel, M.V. Nathal, T.M. Pollock, and D.A. Woodford (TMS, Warrendale, PA, 1996), pp. 101–110.
6. A.M. Wusatowska-Sarnek, M.J. Blackburn, and M. Aindow, *Mater. Sci. Eng. A* **360,** 390 (2003).
7. O.W. Kriege and C.P. Sullivan, Trans. ASM **61,** 278 (1968).
8. O.W. Kriege and J.W. Baris, Trans. ASM **62,** 195 (1969).
9. A. Borgenstam, A. Engström, L. Höglund, and J. Ågren, J. Phase Equilibria **21,** 269 (2000).
10. N. Saunders, *Nickel Database* (Thermotech Ltd., Surrey, U.K., 2001).
11. G. Ghosh (unpublished).
12. J.W. Edington, in *Practical Electron Microscopy in Materials Science* (N.V. Philips, Eindhoven, 1976), pp. 233–236.
13. J.I. Goldstein and H. Yakowitz, in *Practical Scanning Electron Microscopy* (Plenum Press, New York, 1975), p. 86.
14. M.J. Blackburn and R.A. Sprague, Metals Technology **4,** 388 (1977).
15. I. Ansara, T.G. Chart, A. Fernández Guillermet, F.H. Hayes, U.R. Kattner, D.G. Pettifor, N. Saunders, and K. Zeng, CALPHAD **21,** 171 (1997).
16. H. Zapolsky, C. Pareige, L. Marteau, D. Blavette, and L.Q. Chen, CALPHAD **25,** 125 (2001).
17. C.T. Sims, *Superalloys II*, edited by C.T. Sims, N.S. Stoloff, and W.C. Hagel (John Wiley and Sons, New York, 1987), p. 225.
18. A.K. Sinha, in *Progress in Materials Science*, edited by B. Chalmers, J.W. Christian, and T.B. Massalski (Pergamon Press, Oxford, U.K., 1972), Vol. 15, p. 79.
19. H.E. Collins and R.J. Quigg, Trans. ASM **61,** 139 (1968).
20. G.B. Olson, *PrecipiCalc* (Questek, Evanston, IL, 2002).